RSC Advances

PAPER

View Article Online
View Journal | View Issue

Cite this: *RSC Adv.*, 2025, **15**, 50666

Synergistic design of an NiCo@BC–MOF derivative for enhanced energy storage and photocatalytic applications

Malaika Arshad,[a] Zia Ul Haq Khan, *[a] Maryam Zahid[a] and Mahmood M. S. Abdullah [b]

Received 27th October 2025
Accepted 2nd December 2025

DOI: 10.1039/d5ra08231e

rsc.li/rsc-advances

Next-generation energy storage systems demand the development of advanced functional materials. This study synthesizes an NiCo@BC–MOF derivative *via* a hydrothermal route using a 2,5-dihydroxyterephthalic acid ligand. This emerging approach reduces the MOF intrinsic conductivity and enhances structural stability due to synergistic MOF and biochar interactions. The prepared NiCo@BC–MOF exhibited a specific capacitance of 444.44 F g^{-1} at 0.8 A g^{-1}, which decreased to 322 F g^{-1} at higher current density. Furthermore, energy and power densities of 31.96 Wh kg^{-1} and 287.64 W kg^{-1} were also recorded. In addition to electrochemical testing, the material was further identified as a photocatalyst. A pronounced degradation efficiency of 90.1% was achieved for the NiCo@BC–MOF derivative under optimal conditions (pH = 5, catalyst dose = 0.05 g L^{-1}, temp. = 45 °C, and AMX conc. = 50 ppm). The reaction followed pseudo-second-order kinetics and the composite showed good cyclic stability over initial three cycles.

Introduction

Fossil fuels' ongoing depletion contributes significantly to the global energy crisis and underscores a pressing need for clean and reliable energy solutions.[1–4] Traditional renewable and non-renewable sources (wind turbines, solar cells and fossil fuels) serve as viable energy storage options but their effectiveness is often limited due to harsh weather conditions, insecure transportation and high cost.[5] Recently, supercapacitors (SCs) have attracted notable interest owing to their high durability, good reversibility and remarkable power density.[6] The concept of capacitors dates to 1740, when Ewald Georg von Kleist created the first known capacitor device, and later the first commercial appearance of a SC was made by Nippon Electric Company in 1978.[7] Despite considerable progress, designing electrode materials with improved performance suitable for real-world SC applications remains a major challenge, and also poses a key barrier to meeting future energy demands.[8–10] Until now, a variety of electrode materials, including chalcogenides, MXenes, metal oxides, conducting polymers, and metal–organic frameworks (MOFs), and their modifications, have been proposed to tackle the conductivity issue.[11] Recently, MOFs have attracted huge interest and have been widely explored in catalysis,[12] sensing,[13] gas separation, drug delivery,[14] and energy storage.[15] They have been investigated due to their highly tunable structures, large surface areas, adjustable pore networks, and plentiful active sites that facilitate rapid ion transport and efficient charge accumulation.[16,17] Despite these advantages, MOFs are challenging to employ directly as SC electrodes due to their inherently low conductive properties.[18] MOF derivatives have also attracted interest as they preserve the precursor's structural integrity and benefit materials from the synergistic interaction of diverse components.[19,20] Additionally, pyrolysis of MOFs also yields broadly distributed metal oxides that benefit their electrochemical characteristics in response to the dispersed metallic ions and built-in crystallinity of MOFs.[21] These unique properties make MOFs promising candidates for fabricating porous metal oxides.[22,23] To illustrate this, Cr/Cu–MOF-derived oxides were prepared by the calcination of a MOF precursor, which exhibit a capacitance value of 535.1 F g^{-1} at 0.7 A g^{-1} with 90.3% retention over five thousand cycles.[24] In a related study, a ZrO_2/C-based electrode material achieved a specific capacitance of 241.5 F g^{-1} at 1 A g^{-1}, and the fabricated device demonstrated an E_d of 29 Wh kg^{-1} along with a P_d of 1.5 kW kg^{-1}.[25] Similarly, Ni and Co MOF constructed using 2-methylimidazole ligand has been employed to prepare a Co_3O_4/NiO nanocomposite. The resulting material retained its morphology and crystal nature, with a capacitance of 180.4 F g^{-1} at 0.2 A g^{-1} and good stability. The potential of MOF derivatives as adaptable electrodes is demonstrated by these studies.[26,27] The current investigation focuses on bimetallic nickel and cobalt derivatives, which are known for their distinct and complementary electrochemical traits: nickel MOFs display notable capacitive properties and the cobalt metal offers good

[a]*Department of Chemistry, COMSATS University Islamabad, Islamabad Campus, Park Road, Islamabad, 45550, Pakistan. E-mail: ziaulhaqkhan11@gmail.com*
[b]*Surfactants Research Chair, Department of Chemistry, College of Science, King Saud University, P. O. Box 2455, Riyadh 11451, Saudi Arabia*

reversibility.[28–30] According to earlier research, bimetallic MOFs, which combine two or more metals to create a synergistic effect, are more active than their monometallic counterparts.[31,32] In recent years, scientists have shown considerable focus on synergistic integration of MOFs and carbon-based materials.[33] Biochar obtained from biomass is a most adaptable carbon material owing to its enhanced structural and electrochemical properties. It also ensures beneficial energy storage properties such as exceptional surface area, long-term stability, environmental sustainability and improved capacitance.[34–37] These investigations highlight MOF and biochar integrating strategies and open new avenues. The current study focused on synthesis of an NiCo@BC–MOF derived composite *via* a hydrothermal technique. This innovative approach enhances charge transport, inducing significant interaction between MOF and BC which in turn improves the MOF conductivity. The synthetic method employed here also ensures uniform composition, excellent crystallinity, defined morphology, and stands out as the best.[38,39] NiCo@BC–MOF was further characterized by advanced analytical tools to assess its physiochemical behavior. The electrochemical performance of the composite was systematically evaluated through cyclic voltammetry (CV), galvanostatic charge discharge (GCD), and electrochemical impedance spectroscopy (EIS).

Experimental section

Materials and methods

Materials included biochar, sodium hydroxide (NaOH), deionized (DI) water, ethanol, $Ni(CH_3COO)_2$, also known as nickel acetate, cobalt(II) chloride hexahydrate ($CoCl_2 \cdot 6H_2O$), and 2,5-dihydroxyterephthalic acid.

Preparation of biochar

Corn plants, cultivated from different zones, were used as a BC source, and their biomass was thoroughly washed with DI water to eliminate impurities. To achieve purity and homogeneity, the resulting cleaned biomass was then dried, fragmented, and subjected to sonication for 30 minutes. Following this, the sample was dried in an oven for 24 hours, and then its fine powder was used for further processing. Finally, BC was obtained after pyrolysis of dried powder in a furnace at 550 °C for 90 minutes.[40]

Synthesis of NiCo–MOF

In a typical procedure, the NiCo–MOF was prepared *via* a hydrothermal method as depicted in Fig. 1. Initially, nickel acetate (0.58 g) and 0.58 g of $CoCl_2 \cdot 6H_2O$ were added to 40 mL of DI water with continuous stirring until fully dissolved. Simultaneously, 0.48 g of 2,5-dihydroxyterephthalic acid was added to 60 mL of DI water containing 0.32 g of NaOH, facilitating deprotonation. The two prepared solutions were combined and sonicated for 30 minutes to ensure homogenous mixing. After this, the resulting mixture was placed in a stainless-steel autoclave having a Teflon lining and maintained at 170 °C for 12 hours. After naturally cooling to room temperature, the product was washed multiple times with DI water and ethanol to ensure the removal of any residual reactants. Finally, the purified NiCo–MOF was obtained after freeze-drying.[41]

Synthesis of the NiCo@BC–MOF composite

A hydrothermal route was employed to stimulate composite formation, where previously activated BC was added to the MOF solution and heated at 130 °C. The final product was collected, subsequently rinsed with ethanol and DI water, and then dried for six hours at 60 °C in an oven. In the last step, the sample was calcined at 500 °C for 5 hours in an inert nitrogen atmosphere to prevent unwanted reaction.[42]

Electrode preparation

A homogeneous slurry was formulated by combining active material (80%) with 10% polyvinylidene fluoride, 10% carbon black, and several drops of *N*-methylpyrrolidone. It was stirred overnight and then drop-cast on a Ni foam of 1×1 cm^2. Lastly, the electrode was dried at 60 °C for 8 hours.

Characterization

The morphological and structural analyses were performed at King Saud University (Saudi Arabia) research facilities. The composite was analyzed by employing different analytical methods, including X-ray photoelectron spectroscopy, X-ray diffraction, Fourier transform infrared spectroscopy, thermogravimetric analysis, energy-dispersive X-ray spectroscopy, scanning electron microscopy, transmission electron microscopy, zeta potential measurements, and particle size analysis. Galvanostatic charge discharge, electrochemical impedance spectroscopy, and cyclic voltammetry were used to determine capacitive behavior. The photocatalytic study was carried out using a photoreactor.

Results and discussion

Fourier-transform infrared spectroscopy (FTIR)

FTIR analysis of NiCo@BC–MOF and biochar was carried out in the spectral range between 4000 and 500 cm^{-1}, as presented in Fig. 2. The FTIR results of biochar have been published in our previous paper. Since the same plant source of biochar was used in this study, the FTIR data are presented in our earlier publication.[43] The presence of the surface hydroxyl group is confirmed by a broad absorption band at around 3400 cm^{-1}, which is identified as the OH stretching band[4] and specific bands at 1675 cm^{-1} and 1292 cm^{-1} are attributed to C=O and C–O stretching of carboxylate and hydroxyl groups, respectively, as a result of successful coordination of the biochar with the metal ions. Notably, similar bands were also observed for biochar.[41,44] The spectral band observed at 1396 cm^{-1} corresponds to C–C stretching, while the feature at 1042 cm^{-1} corresponds to C–O–Ni tensile vibration, verifying coordination of Ni ions with biochar. Moreover, the weak absorption bands that appeared at 450–700 cm^{-1} are assigned to vibrational modes of cobalt oxides.[45] In addition, the band observed at 443 cm^{-1} is assigned to the Ni–O stretching mode, signifying the bonding interaction of nickel ions with oxygen sites on the biochar surface.[44] Hence, the FTIR study

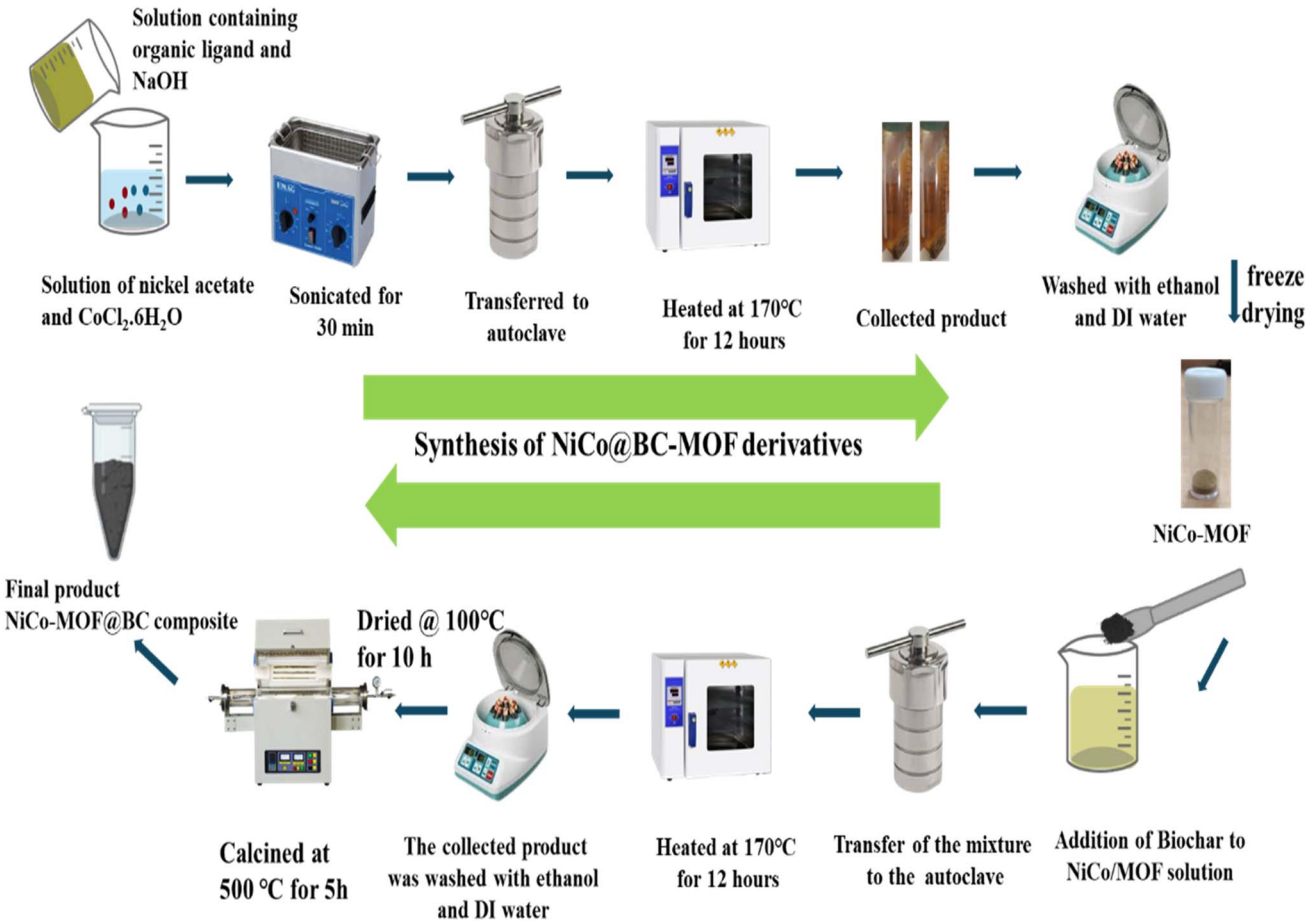

Fig. 1 A schematic illustration of the synthesis of NiCo@BC–MOF.

confirms the synthesis of the NiCo@BC–MOF derivative, highlighting the strong interaction between biochar and metal ions.

X-ray diffraction (XRD)

The sharp, intense, and well-defined peaks as presented in Fig. 3 in advanced XRD confirm the high degree of crystallinity of the NiCo@BC–MOF derivative. Here, the diffraction pattern observed with peaks at $2\theta = 36.96°$, 43.06°, 62.43°, 75.99°, and 79.01° correlated to the Miller indices of (111), (200), (220), (311), and (222), having space group $Fm\bar{3}m$, indicates the presence of NiO. The relative intensities and measured 2θ values show a strong correlation with JCPDS card no. 01-071-1179, further validating phase identification, while the reflections observed at 36.96° (311), 44.41° (400), 74.94° (620), and 78.87° (622) referenced to JCPDS card no. 00-009-0418, having space group $Fd\bar{3}m$, correspond to Co_3O_4. These characteristic peaks confirm the effective integration of mixed oxides (Ni and Co) within the biochar framework, indicative of NiCo@BC–MOF composite synthesis. No additional peaks were detected, indicating the high phase purity of the prepared composite material. Debye–Scherrer analysis revealed that the material possesses an average crystallite size of 8.48 nm:

$$D = \frac{k\lambda}{\beta \cos \theta} \quad \text{(a)}$$

In this equation, D represents the size of crystallites, k is the Scherrer constant, λ is the X-ray wavelength (0.15406 nm), θ is Bragg's angle, and β indicates the full width at half maximum, taken as 0.9.

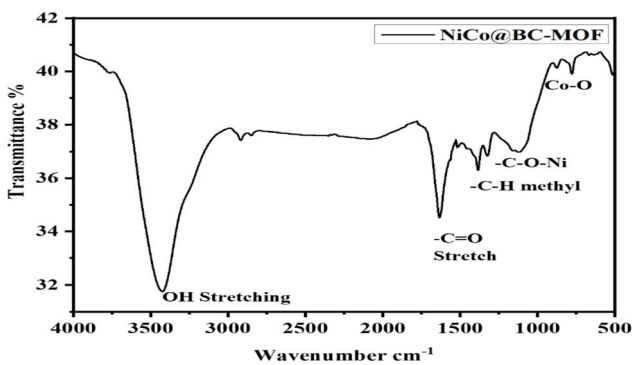

Fig. 2 The FTIR spectrum of NiCo@BC–MOF.

Scanning electron microscopy (SEM)

The morphological characteristics of BC and NiCo@BC–MOF were observed *via* SEM. The SEM results of biochar have been

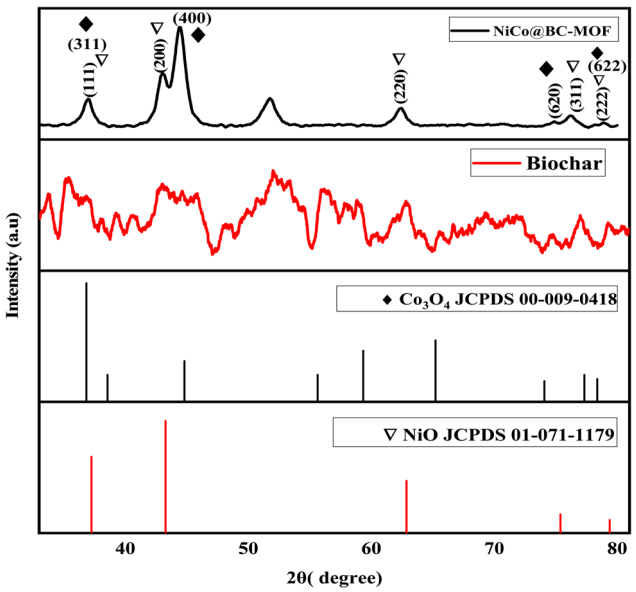

Fig. 3 XRD patterns of biochar (red) and NiCo@BC–MOF (black).

published in our previous paper. Since the same plant source of biochar was used in this study, the SEM results are presented in our earlier publication.[43] SEM analysis of NiCo@BC–MOF (Fig. 4a and b) at a magnification of 5 μm and 10 μm reveals a network of interconnected pores, confirming the successful integration of MOF derivatives within BC. The spherical and irregularly shaped nanoparticles correspond to Ni- and Co-based metal oxides embedded in a biochar matrix having varying sizes, with smaller ones uniformly dispersed while larger ones tend to form some agglomerates on the surface. The high-resolution SEM images demonstrate strong binding interaction between MOF and biochar, reinforcing composite structural stability and hierarchical porosity.[44]

Energy-dispersive X-ray spectroscopy (EDX)

The EDX spectrum of NiCo@BC–MOF in Fig. 4c verifies the elemental makeup and demonstrates the presence of Ni and Co, alongside carbon and oxygen, providing clear evidence of their incorporation into the BC matrix.[46,47] A detailed elemental distribution of the NiCo@BC–MOF derivative is presented in Table 1.

Transmission electron microscopy (TEM)

TEM micrographs of NiCo@BC–MOF in Fig. 5a and b demonstrate that Ni and Co nanoparticles have been fully integrated as spherical and elongated structures into the carbon skeleton of BC. Here, van der Waals and electrostatic forces dictate

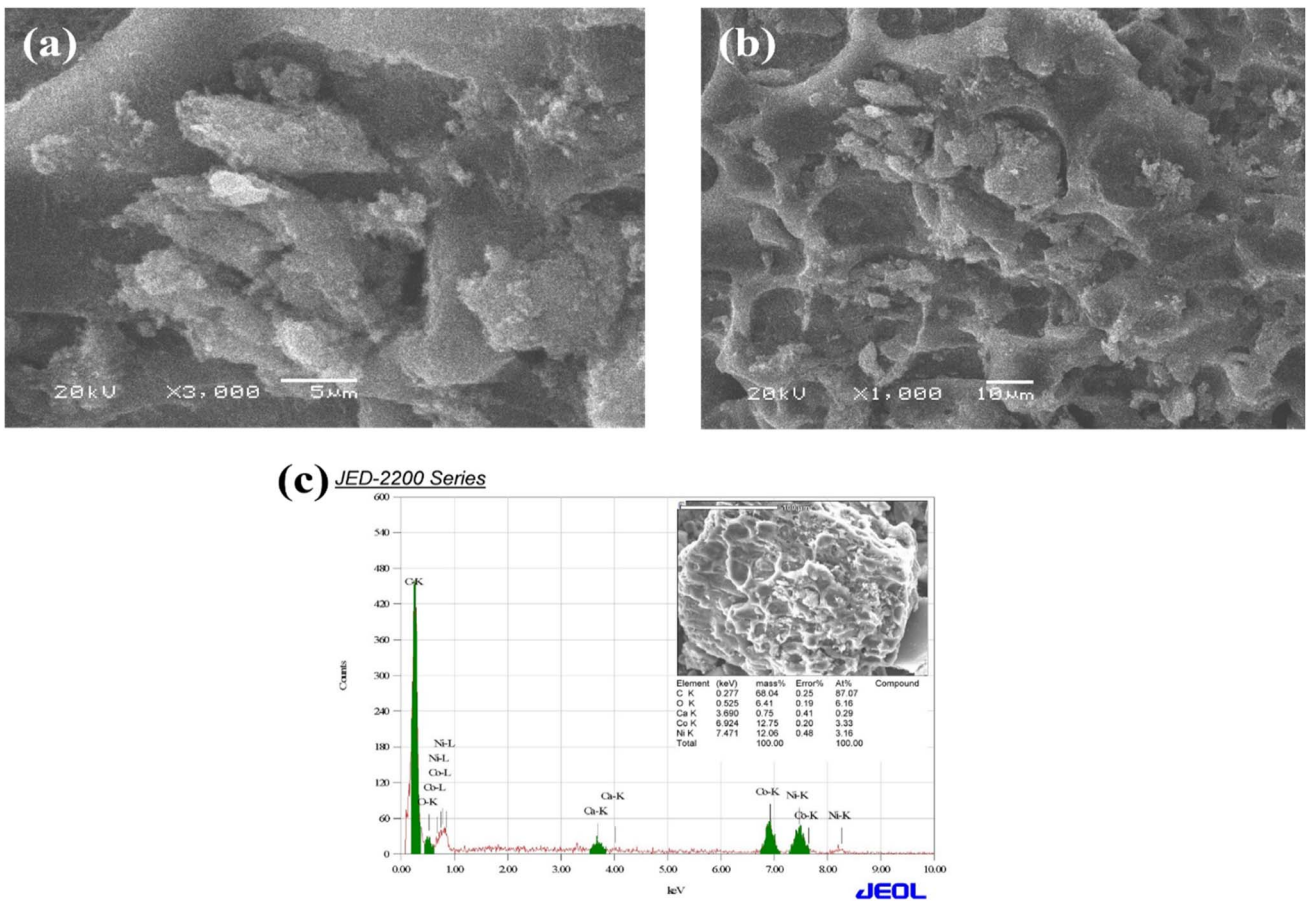

Fig. 4 SEM images of NiCo@BC–MOF (a and b), and the EDX spectrum (c).

Table 1 The elemental distribution of NiCo@BC–MOF

Element	keV	Weight %	Atomic %	Error %
C	0.277	68.04	87.07	0.25
O	0.525	6.41	6.16	0.19
Ca	3.690	0.75	0.29	0.41
Co	6.924	12.75	3.33	0.20
Ni	7.471	12.06	3.16	0.48
Total		100.00	100.00	

clustering of these nanoparticles to provide effective dispersion and stability. This distinctive structure validates the unique and improved electrochemical properties.[44] The histogram in Fig. 5c represents the particle size distribution derived from TEM images. It suggests that most particles are of small size, having an average particle size of 11.58 nm.

Thermogravimetric analysis (TGA)

TGA presents a two-step weight loss profile in the 30–800 °C temperature interval, as displayed in Fig. 6. Here, the initial loss of 3.97% below 200 °C is attributed to loss of absorbed water, moisture, or residual solvent within the material structure. A pronounced weight reduction (6.25%) between 350 and 500 °C may be due to the oxidation of some unstable residual carbon or decomposition of oxygen-containing functionalities.[48–50] Thus, TGA shows good thermal stability, and the overall weight loss is 10.22%, indicating that most of the material is not lost and can be used at elevated temperatures.

Zeta potential (ZP)

A ZP value of −9.93 mV as presented in Fig. 7 indicates low repulsive forces that sometimes lead to aggregation in colloidal suspensions. Although such a ZP value suggests that particles are inclined to form aggregates, this drawback can be addressed by using appropriate techniques. The adhesion of active material to the electrode is improved by the use of a binding agent, and the even dispersion of aggregates is facilitated by sonication.[51,52]

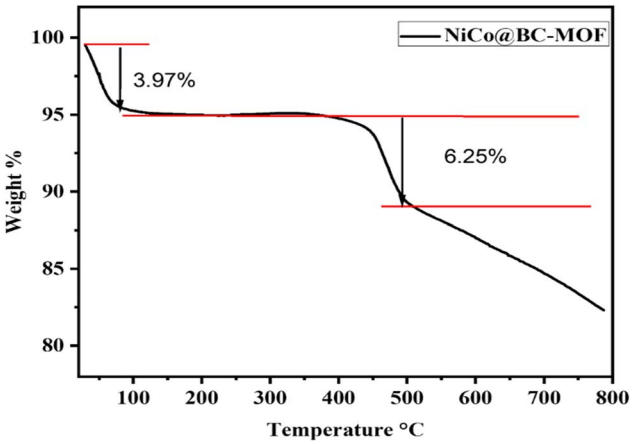

Fig. 6 The TGA curve of NiCo@BC–MOF.

X-ray photoelectron spectroscopy (XPS)

The composition and oxidation state of the elements on the surface of the synthesized composite were analyzed using XPS. The XPS survey spectrum in Fig. 8a shows clear peaks of Ni 2p, Co 2p, C 1s, and O 1s, confirming that Ni and Co oxides have been successfully incorporated in the biochar structure, and this is also confirmed from the high-resolution spectra. As illustrated in Fig. 8b, the C 1s spectrum exhibits a sharp peak at 286.0 eV corresponding to C–O bonding, suggesting the existence of oxygenated functional groups. The O 1s spectrum,

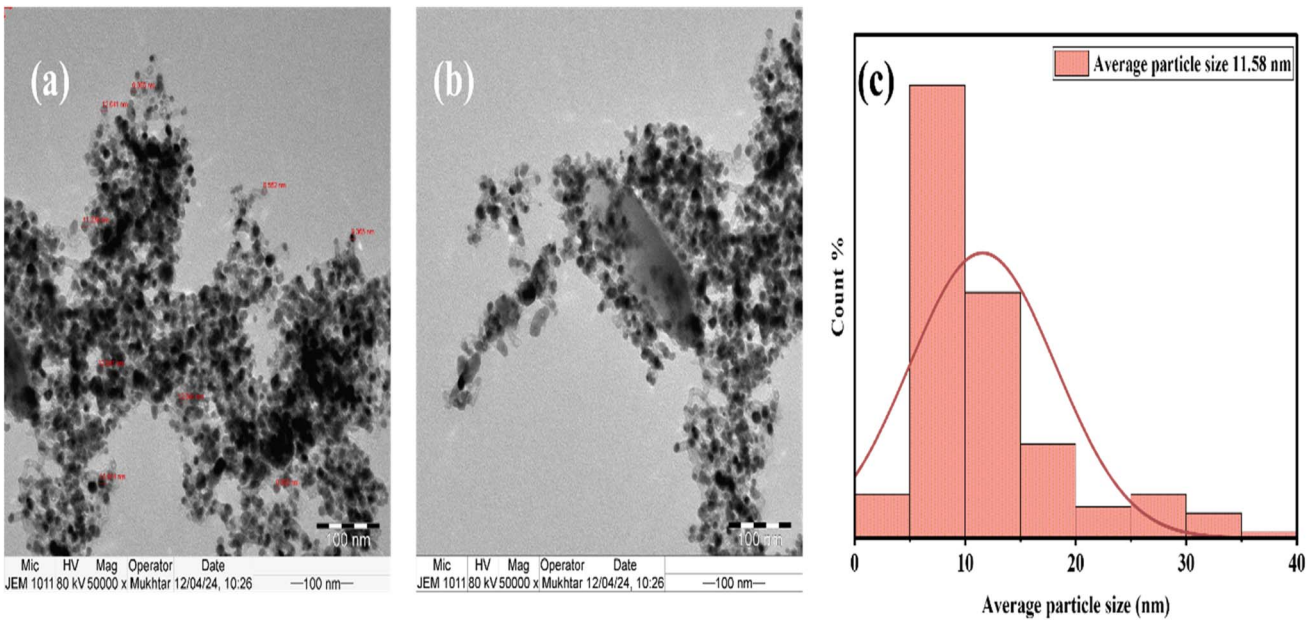

Fig. 5 TEM images of NiCo@BC–MOF (a and b), and a particle size histogram (c).

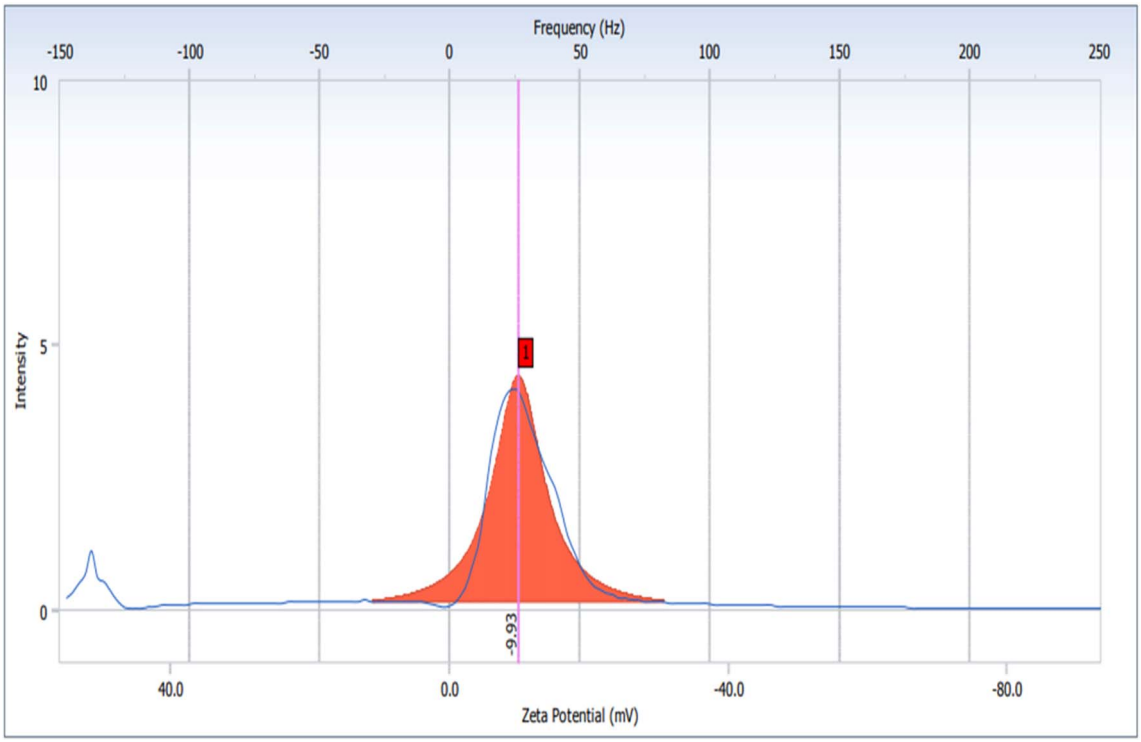

Fig. 7 ZP measurements of NiCo@BC–MOF.

Fig. 8c, shows peaks at 532.1 eV and 533.0 eV, which can be linked to metal–oxygen interactions.[53] Spin–orbit coupling causes the Ni 2p and Co 2p orbitals to split into two distinct energy states, identified as $2p_{3/2}$ and $2p_{1/2}$. In Fig. 8d, the Co 2p spectrum displays two main peaks at binding energies of 779.0 eV (Co $2p_{3/2}$) and 795.6 eV (Co $2p_{1/2}$), accompanied by

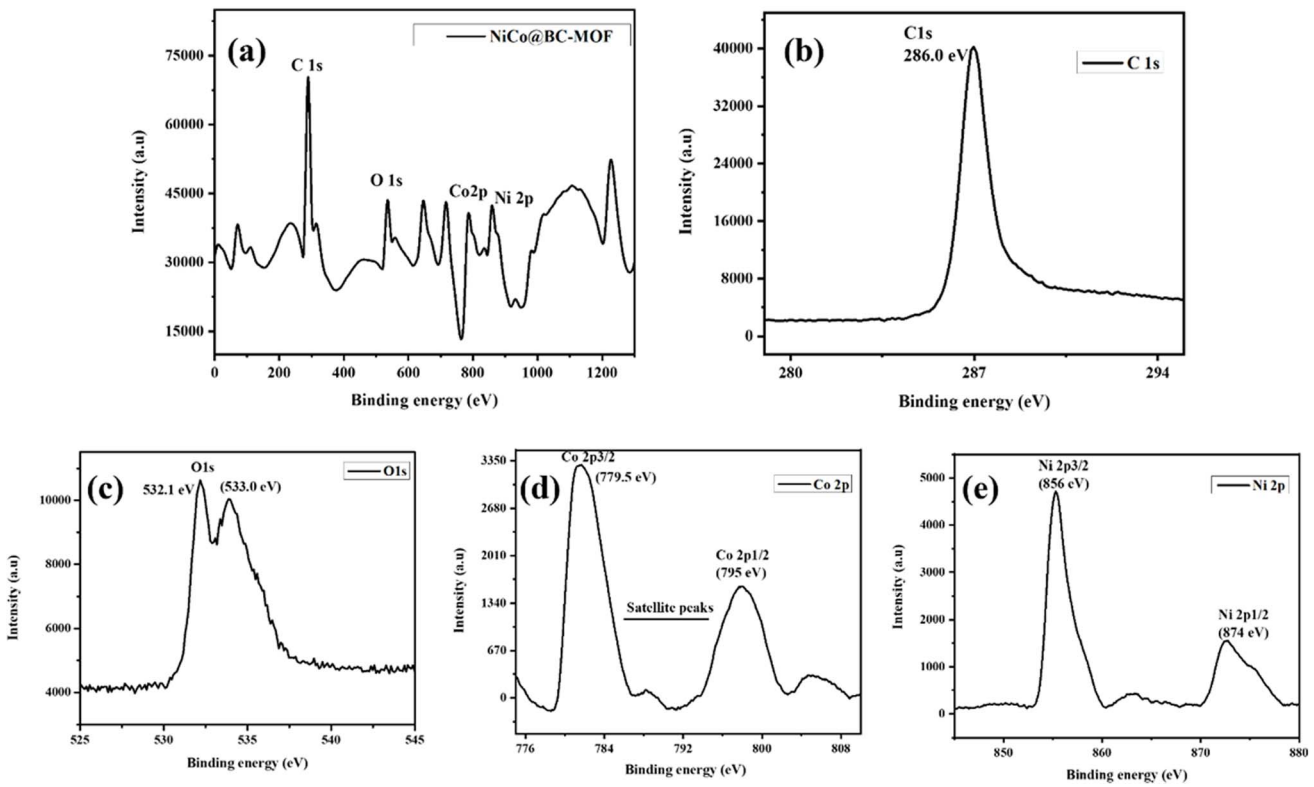

Fig. 8 XPS spectra of NiCo@BC–MOF: survey spectrum (a), and carbon 1s (b), oxygen 1s (c), cobalt 2p (d), and nickel 2p (e) spectra.

satellite peaks, confirming the coexistence of Co^{3+} and Co^{2+} oxidation states. Likewise, the Ni 2p spectrum has two strong peaks, which correspond to Ni $2p_{3/2}$ and Ni $2p_{1/2}$. The fitted peaks at 856.6 eV are assigned to Ni^{3+}, while that at 875.5 eV suggests the presence of Ni^{2+}. These XPS results are in agreement with EDX findings.[54]

Particle size analysis (PSA)

PSA was conducted to define the average particle size and properties further. The intensity distribution graph in Fig. 9a exhibits dominant primary peaks having an average particle size of 854.9 nm with a standard deviation (SD) of 1165.7. Meanwhile, the volume distribution graph in Fig. 9b gives an insight into the contribution of the various particle sizes to the total sample volume. The graph of volume distribution recorded a value of 2044.3 nm, having SD of 840.1. It highlights the relatively uniform size distribution of particles. In Fig. 9c, the number distribution graph represents an average size of 133.1 nm with SD of 132.2. A narrower size range with main peaks leaning towards smaller particles indicates that the smaller particles are abundant, confirming that the synthesis process successfully generated a consistent size required for an electrode material. While Fig. 9d shows an logarithmic plot displaying smooth decay curves having a polydispersity index of 0.272, confirming good dispersion, minimal aggregation, and stability of NiCo@BC–MOF.[55]

Electrochemical application

Electrochemical performance of the obtained material was monitored by performing CV, GCD, and EIS measurements in 2 M KOH solution using a three-electrode setup. Here, platinum wire was used as a counter electrode, while Ag/Ag served as a reference.

Cyclic voltammetry

CV was used to characterize the fabricated material based on the redox reactions of the material. The cyclic voltammograms of the bare electrode and NiCo@BC–MOF, recorded at scan rates of 20 and 30 mV s^{-1}, are displayed in Fig. 10a. The CV plots of NiCo@BC–MOF show large areas signifying a higher capacity. The increase in the capacity is said to be due to both nickel and cobalt metal ions participating in the faradaic reaction in a charge–discharge cycle. The CV profiles reveal noticeable oxidation and reduction peaks at 0.48 V and 0.14 V, respectively, signifying the reversible faradaic transitions of Ni^{2+}/Ni^{3+} and Co^{2+}/Co^{3+}, through the following possible reactions:

$$NiO + OH^- \rightleftharpoons NiOOH + e^-$$

$$Co_3O_4 + OH^- + H_2O \rightleftharpoons CoOOH + e^-$$

With increasing scan rate, the anodic and cathodic peak separation increases, indicating diffusion-controlled faradaic processes, while the quasi-rectangular background suggests

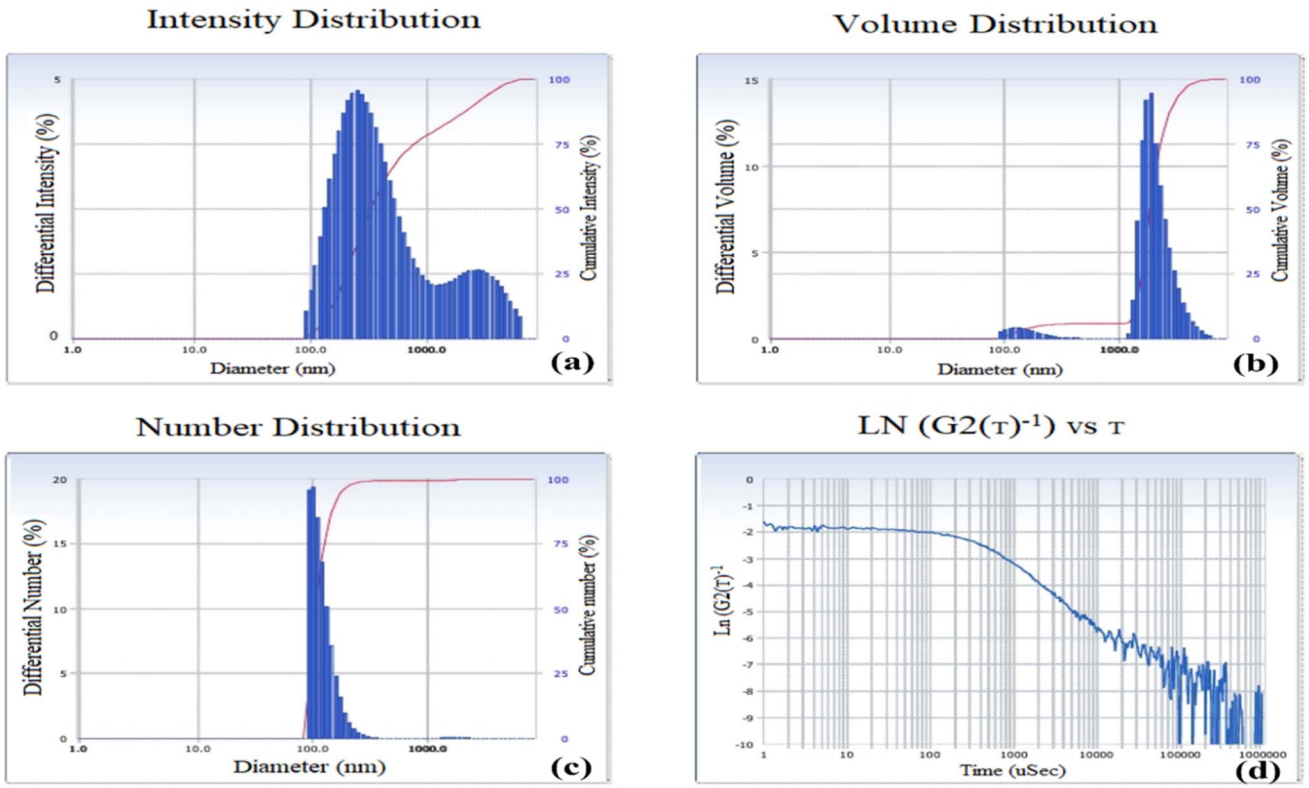

Fig. 9 Particle size analysis of NiCo@BC–MOF. (a) Intensity distribution, (b) volume distribution, (c) number distribution, and (d) logarithmic plot.

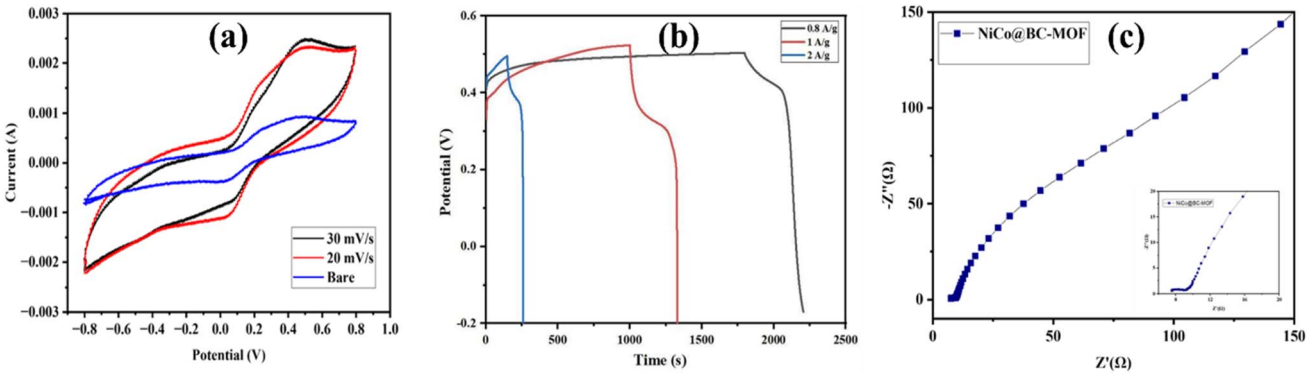

Fig. 10 (a) CV curves at 20 and 30 mV s^{-1}. (b) GCD curves at varying current densities. (c) EIS results of NiCo@BC–MOF.

a concurrent surface capacitive contribution. These observations demonstrate that the electrochemical behavior of NiCo@BC–MOF arises from a constructive combination of faradaic and capacitive mechanisms. Here, the area of the cyclic voltammogram as well as GCD nonlinear curves confirm that the storage mechanism is due to faradaic redox reaction and additional surface capacitive properties of BC. The semicircle observed in the EIS plot further indicates low charge transfer resistance and efficient transport. In general, NiCo@BC–MOF exhibits a synergistic mechanism involving pseudocapacitive and diffusion-controlled processes.[56]

Galvanostatic charge discharge (GCD)

GCD identifies the electrochemical properties by feeding a constant current to the electrode material over a specific time period and then discharging it at a continuous rate. This testing, therefore, requires a steady current of charging and discharging. GCD curves feature nonlinearity, signifying pseudocapacitive behavior caused by redox reaction. The *iR* drop seen at the start of all discharge curves is due to considerable internal resistance during the rapid charge–discharge process. The behavior at different current densities, 0.8, 1, and 2 A g^{-1}, was evaluated through GCD measurements, as presented in Fig. 10b. The discharge period of the electrode decreased from 400 s to 113 s as the current density increased from 0.8 to 2 A g^{-1}. The electrode delivered specific capacitances of 444.44, 416.66, and 322 F g^{-1} at respective current densities of 0.8, 1, and 2 A g^{-1}, calculated using the following equation:

$$C_s = \frac{I \times DT}{\text{active}_{\text{mass}} \times \Delta V}$$

The gradual decrease is mainly due to the restricted accessibility of electrolyte ions to active sites within the porous structure.[57] Energy densities of 31.96, 29.99, and 23.18 Wh kg^{-1} were obtained at varying current densities, along with power densities of 287.64, 359.99, and 738.6 W kg^{-1}, respectively. All these results confirm the good electrochemical performance of the synthesized composite.

Electrochemical impedance spectroscopy

EIS measurement was performed to analyze the charge transport properties associated with energy storage and water splitting. In EIS, the Nyquist plot and Bode phase plots result from impedance in the 100 kHz to 10 MHz frequency range of current required to study the resistance of electrolyte solutions. To further verify the electrochemical behavior of NiCo@BC–MOF, EIS was carried out, and the Nyquist plot is presented in Fig. 10c. EIS analysis reveals a high-frequency semicircle followed by a low-frequency linear region. The semicircle represents resistance resulting from charge transport at the electrode interface.[58,59] A smaller diameter of the semicircle indicates a low R_{ct} value of NiCo@BC–MOF. The interaction between Ni and Co enhances conduction, accelerates charge discharge, and therefore minimizes resistance. Moreover, inclusion of biochar in the form of a conductive support enhances the effect by offering a conductive substrate. Following the electrochemical evaluation, a comparison with some reported MOF-based electrodes is presented in Table 2. The NiCo@BC–MOF electrode delivers a specific capacitance of (444.44 F g^{-1} at 0.8 A g^{-1}). This enhanced performance can be explained by the synergistic redox activity of ions of Ni and Co, which improves the reversible faradaic reactions, and the presence of biochar, which gives a highly conductive and porous skeleton that facilitates the

Table 2 Electrochemical performances of various MOF-based composites

No.	Electrode material	Synthetic route	Capacitance	Ref.
1	2D layered Ni–MOF	—	184 F g^{-1} at 0.5 mV s^{-1}	60
2	Co BTC MOF	Hydrothermal	261.27 F g^{-1}	61
3	Co/Ni–MOF-1 : 15	Solvothermal	359 F g^{-1} at 0.5 A g^{-1}	62
4	2D NiCo–MOF/GO	Ultrasonic	413.61 C g^{-1} at 0.5 A g^{-1}	63
5	NiCo@BC–MOF	Hydrothermal	444.44 F g^{-1} at 0.8 A g^{-1}	This work

movement of charges and ions. In addition, the hydrothermal route provides uniform particle growth and well-bonded surfaces, which leads to better structural integrity and electrochemical stability, in comparison to electrodes described earlier.

Photocatalytic study

Rapid industrialization and economic growth have intensified environmental and energy challenges, creating significant barriers to sustainable development, while the discharge of industrial wastewater further aggravates these issues by threatening ecosystems, public health, and industrial operations.[64,65] In the pharmaceutical industry, antibiotic intake has been on an upward trend with enormous potential to treat multiple human and veterinary infections. These drugs are chemically complex and resistant to biodegradation, resulting in partial digestion in humans and the release of residual compounds into environmental matrices.[43,66] In recent years, numerous techniques have been implemented to remove and degrade pollutants in different media, such as adsorption, photo-electrocatalysis, biodegradation, electrochemical treatment, photocatalysis, and advanced oxidation. Among them, photocatalysis serves as a promising tool and has gained immense popularity as a sustainable and eco-friendly technique using sunlight.[67,68] Recently, MOFs have evolved as a growing tool of interest in photocatalysis. Compared to traditional metal oxide semiconductors, MOFs have diverse advantages such as large surface area, good topology, and porous structure, which can be easily engineered.[69] This paper explores the potential of the synthesized composite to degrade the amoxicillin (AMX) drug. The effect of different parameters, including pH, catalyst concentration, drug concentration, and temperature, was studied. Further, cyclic stability was also verified. AMX is a widely prescribed broad-spectrum β-lactam antibiotic that belongs to the aminopenicillin class. It is widely used to treat various bacterial infections, such as those of the respiratory system, urinary tract, and skin, as well as some gastrointestinal infections.[70] Its long-term resistance, gradual decay, and the possibility of causing antibiotic resistance in microorganisms are of great environmental concern, especially in terms of water pollution and human health.[71,72] Traditional wastewater treatment techniques are typically ineffective in getting rid of such persistent pharmaceutical pollutants. To tackle this issue, a variety of MOF-based catalysts, such as Co–MOF(DABCO) and a bimetallic NiCo–MOF(DABCO), were synthesized, and their photocatalytic performance was tested against cefoperazone (CP) following visible light illumination.[73] NiCo–MOF(DABCO) demonstrated better performance, showing a larger degradation rate constant (7.4×10^{-3} min^{-1}), as compared to Co–MOF(-DABCO) (5.3×10^{-3} min^{-1}). Optimization using the response surface method reached 88.9% CP removal, and the catalyst was stable even after five repeat cycles.[74] In addition to this, MIL-68(In)–NH_2/graphene oxide was also employed as a photocatalyst to degrade AMX. The composite demonstrates high degrading activity under optimum conditions, compared to pristine MIL-68(In–NH_2), at 93% AMX removal.[75] Based on these investigations, the NiCo@BC–MOF composite was also identified as a photocatalyst. The coexisting Ni and Co ions here create abundant redox active sites that effectively reflect light and transfer charge. The newly established cooperation is a promising strategy for the long-term degradation of AMX in water.

Photodegradation setup

A 10 ppm AMX solution was prepared as a standard, and 0.1 M H_2SO_4 and NaOH were employed to adjust its pH. In the optimized photocatalytic analysis, 0.05 g L^{-1} of composite was added to AMX solution (50 ppm), and the sample was placed in the dark for 30 minutes to establish adsorption–desorption equilibrium. Furthermore, a 20 W lamp placed 10 cm above the vessel was used to expose the reaction mixture to visible light. Aliquots were collected every 5 minutes, centrifuged at 10 000 rpm for 10 minutes, and the concentration of AMX was measured using a UV-visible spectrophotometer at 273 nm. The influence of varying AMX concentrations was examined by conducting experiments with 10, 20, 30, 40, and 50 mg L^{-1} solutions under the same conditions. Kinetic experiments were conducted at a 10 mg per L AMX level, and the samples were taken every 5 min; the catalyst dosage was kept constant at 50 mg L^{-1}. Next, the efficiency of NiCo@BC–MOF in the degradation process was determined by using eqn (1):

$$R\ (\%) = \left(\frac{C_0 - C_f}{C_0}\right) \times 100 \quad (1)$$

where C_0 represents the initial concentration of the drug (mg L^{-1}) and C_f the final drug concentration (mg L^{-1}).

Kinetic modeling

The degradation kinetics of AMX were evaluated using the pseudo-first-order (PFO) kinetic model, the pseudo-second-order (PSO) model, and the Langmuir–Hinshelwood model, as represented in eqn (2)–(4).

$$\frac{\ln C_0}{C_t} = k_{obs} t \quad (2)$$

where C_0 refers to the initial pollutant concentration, t is the reaction time, and k_{obs} represents the rate constant for PFO.

$$\frac{t}{C_t} = \frac{1}{k_2 {C_e}^2} + \left(\frac{1}{C_e}\right) t \quad (3)$$

where C_t (mg g^{-1}) represents AMX adsorbed at time t, k_2 (g mg^{-1} min^{-1}) is the PSO rate constant, and C_e (mg g^{-1}) denotes the equilibrium adsorption capacity.

$$\frac{1}{r_0} = \frac{1}{k_r} + \frac{1}{k_r K C_0} \quad (4)$$

Here, r_0 denotes the initial reaction rate, C_0 is the initial concentration of the drug, k_r refers to the rate constant for the Hinshelwood model, and K corresponds to the equilibrium binding constant.

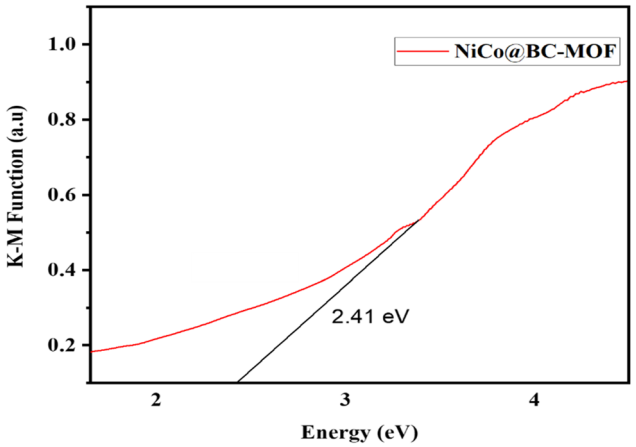

Fig. 11 Band gap analysis of NiCo@BC–MOF.

Band gap

The Tauc plot was used to estimate the band gap of the material, where the absorption coefficient is associated with indirect electronic transitions. (*i.e.*, the energy band gap, E_g):

$$(\alpha h\nu)^r \propto h\nu - E_g \quad (5)$$

where h denotes Planck's constant, ν represents the frequency for indirect transitions, r is 1/2, and the energy corresponding to the wavelength was computed using the following equation:

$$E_g = hc/\lambda \quad (6)$$

In this case, λ is the wavelength and c is the speed of light. The slope of the Tauc plot was used to estimate the band gap by extrapolating the slope to the x-axis, yielding a value of 2.41 eV, as shown in Fig. 11. The reduced band gap enhances the photocatalytic activity by facilitating the efficient generation of charge carriers.

pH effects

pH is a crucial factor affecting the photodegradation of AMX. To assess its impact, experiments were conducted at pH values of 5, 6, 7, 8, and 9, while all other experimental parameters were kept constant. The impact of pH on AMX catalytic degradation with NiCo@BC–MOF is presented in Fig. 12a. The results show that the highest degradation of AMX, 90.0%, was obtained at pH 5 within 30 minutes, thus showing that weakly acidic conditions of pH 5 provide the most promising environment in agreement with previous studies.[76,77] Conversely, the catalytic activity decreased progressively with rising pH, showing reduced activity under alkaline conditions at pH 9. This tendency can be

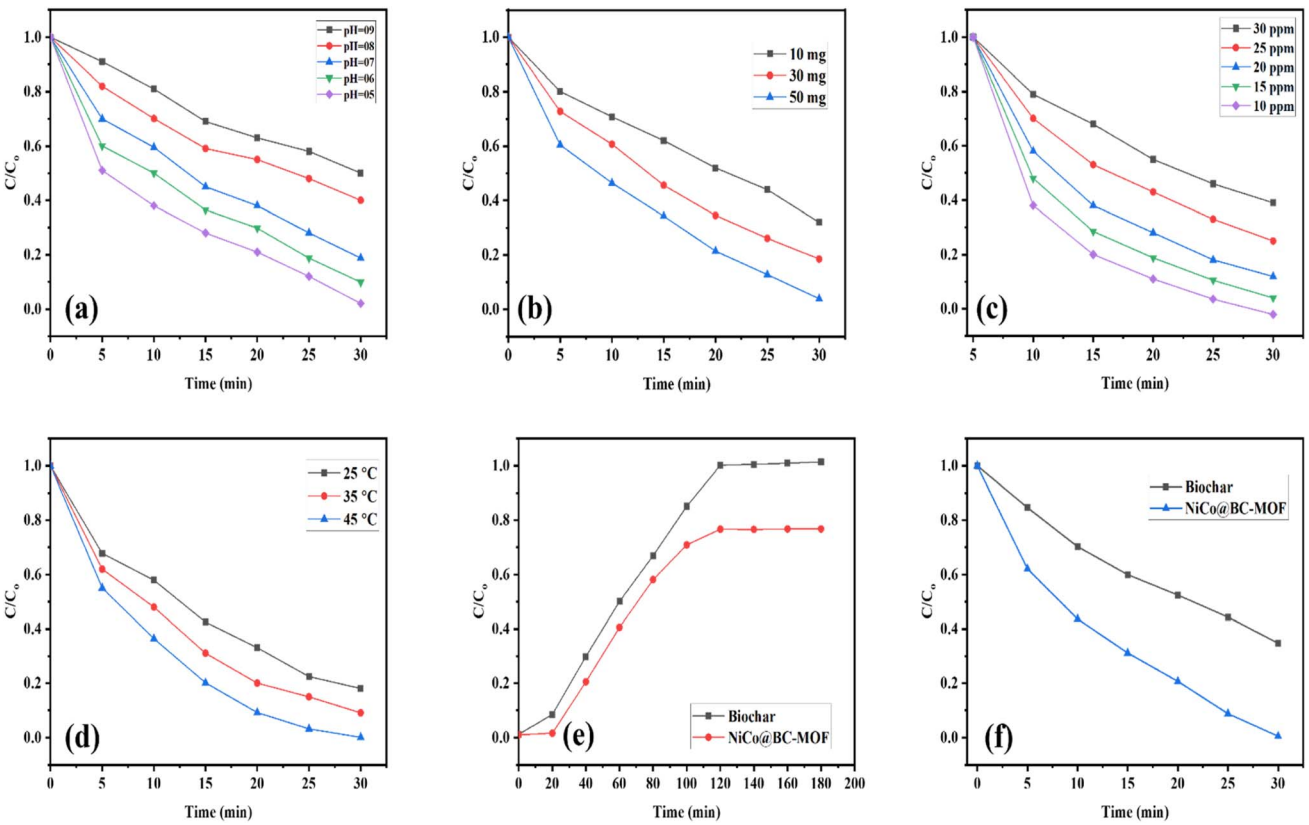

Fig. 12 AMX degradation studied with respect to pH (a), catalyst amount (b), AMX concentration (c), temperature (d), and reaction time (e). (f) Comparison of the performances of BC and NiCo@BC–MOF under optimized conditions (pH 5; catalyst: 50 mg; AMX concentration: 10 mg L^{-1}; temperature: 45 °C).

explained by electrostatic interaction between AMX (as a cation at pH 5) and the NiCo@BC–MOF surface (negatively charged): these interactions result in an effective transfer of charge and activation of the antibiotic. Adsorbed AMX is readily oxidized by reactive oxygen species (ROS), *e.g.*, superoxide radicals ($O_2^{\bullet}$) and hydroxyl radicals ($OH^{\bullet}$) formed due to excitation of NiCo@BC–MOF under light conditions. In contrast, neutral and alkaline conditions promote the deprotonation of AMX and, thus, inhibit ROS-catalyzed degradation by decreasing the binding affinity to the catalyst surface.[75,78] These findings provide validity to the assumption that pH regulates the adsorption potential, directly influencing the pathways of the catalytic reaction, where acidic conditions (pH 5) are more favorable for efficiently removing AMX. The following schematics depict the electronic transfer that is usually involved in ROS formation:[79,80]

$$\text{NiCo@BC–MOF} + h\nu \rightarrow {e_{CB}}^- + {h_{VB}}^+$$

$$O_2 + {e_{CB}}^- \rightarrow {}^{\bullet}O_2^- \text{ and } 2{}^{\bullet}O_2 + 2H^+ \rightarrow H_2O_2 + O_2$$

$$e^- + H_2O_2 \rightarrow {}^{\bullet}OH + OH^-$$

or

$$h^+ + H_2O_2 \rightarrow H^+ + {}^{\bullet}OH$$

$$Ni^{3+} + e^- \rightarrow Ni^{2+},\ Co^{3+} + e^- \rightarrow Co^{2+}$$

$${}^{\bullet}OH + {}^{\bullet}O_2^- + \text{AMX} \rightarrow \text{intermediates} \rightarrow CO_2 + H_2O + \text{inorganic ions}$$

Dosage of NiCo@BC–MOF

A photocatalytic investigation, as illustrated in Fig. 12b, using dosages ranging from 10 to 50 mg L^{-1}, was used to assess the impact of catalyst amount in AMX removal. It has been demonstrated that raising the catalyst dosage significantly improved the photodegradation efficiency because more functional sites were accessible, providing a large surface area for incoming photon interaction.[81,82]

Amoxicillin concentration

The effect of AMX level was examined through experiments employing concentrations ranging from 10 to 50 ppm. As the pollutant level increased, the photodegradation efficiency progressively decreased, as indicated in Fig. 12c.[83,84] The decreased degradation rates at elevated concentrations can be explained by several factors, such as the adsorption of drug molecules in more than one layer, subsequent deactivation of active sites, internal diffusion resistance, and inhibition of $^{\bullet}OH$ formation.[85,86]

Temperature effects

The temperature of the reaction is also a principal factor that dictates the rate of pollutant removal. An increase in temperature from 25 to 45 °C resulted in a significant rise in the photodegradation rate of AMX (Fig. 12d). This enhancement is credited to the increased thermal activation of drug molecules, which promotes more frequent and effective collisions with NiCo@BC–MOF. Additionally, elevated temperatures improve the mobility of photogenerated electron pairs, which in turn facilitates AMX transfer. The enhanced temperature also stimulates the formation of ROS, contributing to more efficient degradation of AMX.[87,88]

Contact time

The influence of reaction time was also investigated, as presented in Fig. 12e, where the black curve represents bare BC and the red one the NiCo@BC–MOF composite. It is observed that the degradation efficiency of BC is decreasing and increases slowly with time to a lesser plateau point, which could be attributed to its adsorption capacity rather than its photocatalytic activity. On the contrary, NiCo@BC–MOF exhibits a rapid increase in the degradation rate during the first reaction period and reaches a higher maximum removal. This can be attributed to the cooperative effect of biochar and the bimetallic Ni/Co–MOF that improves visible light absorption and provides a higher number of active sites. These results confirm that incorporation of NiCo–MOF in the biochar skeletal scaffold is effective in promoting the photocatalytic activity in line with previous research, where MOF-based composites facilitate a greater degradation performance compared to their counterparts.[89]

Comparative analysis of optimized parameters

Comparison between the photocatalytic activity of NiCo@BC–MOF and biochar is presented in Fig. 12f. The composite reached a peak degradation rate of 90.1% and biochar had a lower removal rate of 65.25%. The composite employed in this study was synthesized through a straightforward hydrothermal process, and it has an outstanding photocatalytic degrading potential, environmental friendliness, high stability, and a high surface area.[90] The synergistic combination of Ni/Co bimetallic active sites with conductive biochar enabled better charge separation and faster ROS generation, improving the photodegradation reaction. Moreover, the material retained most of its catalytic activity after multiple reuse cycles, indicating good stability.

Reusability

The recyclability of the NiCo@BC–MOF composite when used for the degradation of AMX was examined under consecutive photocatalytic cycles, and the outcome is shown in Fig. 13a. The result of filtration obtained after every cycle was washed and then examined using UV-visible spectroscopy to evaluate the degradation efficiency. During the initial cycle, the catalyst exhibited the most efficient removal rate of almost 85%, which validated its high activity. When the composite was reused in the second and third cycles, the performance did not decrease significantly, demonstrating that most activity was retained by the composite in the first three runs. However, there was a more noticeable decline, with efficiency falling to about 65% in the fourth cycle and 40% by the end of the fifth cycle.[85,91] This

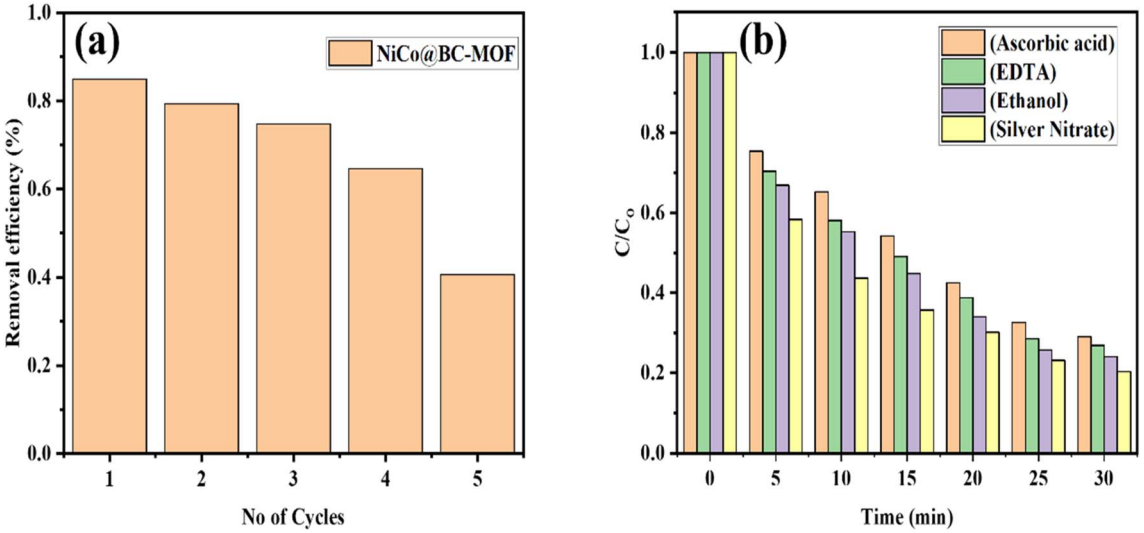

Fig. 13 (a) Recyclability and (b) the influence of radical scavengers (ascorbic acid, EDTA, ethanol, and silver nitrate) on AMX degradation.

gradual decline in activity can be explained by the potential loss of active Ni and Co sites, blockage by degradation intermediates, partial structural instability of the MOF framework, and inevitable loss during recovery processes.[84] Consequently, the overall activity of the material diminished markedly, resulting in less of a contribution to drug removal.

Scavenger study

The primary ROS contributing to AMX photocatalytic degradation were investigated through scavenger trapping studies on NiCo@BC–MOF. Ethanol was employed as a scavenger for hydroxyl radicals ($^{\bullet}OH$), while ethylenediaminetetraacetic acid (EDTA) and silver nitrate were used to scavenge holes (h^+) and electrons (e^-), respectively. Ascorbic acid was employed to scavenge superoxide ions ($^{\bullet}O_2^-$). The addition of ascorbic acid resulted in the greatest inhibition of photocatalytic efficiency, Fig. 13b, which implied that the most predominant ROS were superoxide radicals. Comparatively, EDTA and ethanol had moderate effects, indicating that photogenerated holes and hydroxyl radicals have secondary though important effects. Silver nitrate produced the least inhibition, which indicates that electrons played a small role in the degradation. These findings verify that ($^{\bullet}O_2^-$) is the competitive driver of the photocatalytic process, supported synergistically by ($^{\bullet}OH$) and (h^+).[92,93]

Kinetic modeling

The photocatalytic degradation process was evaluated through kinetic modeling using PFO, PSO, and Langmuir–Hinshelwood approaches, as shown in Fig. 14a–c. Among the applied models, the experimental results exhibited good agreement with the PSO model. Table 3 summarizes the kinetic rate constants and their corresponding correlation coefficients (R^2).

Proposed degradation pathway

Fig. 15 shows schematically the photocatalytic degradation mechanism of AMX in the presence of the NiCo@BC–MOF composite. When the photocatalyst is irradiated with light, photons are absorbed and create electron–hole pairs, where the electrons in the photocatalyst are excited to the conduction band, and the holes remain in the valence band. The presence of biochar offers an effective electron-conducting network capable of capturing and transmitting photogenerated electrons, thereby

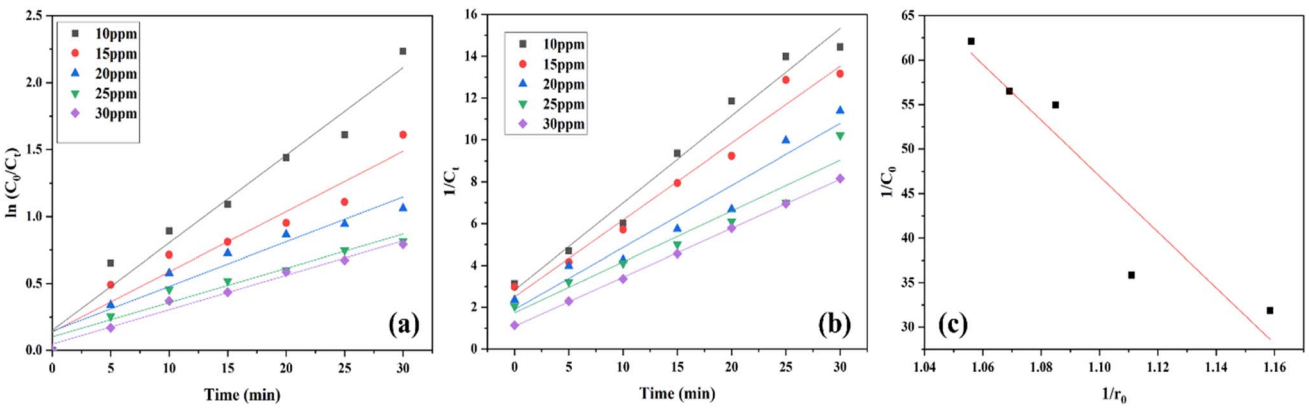

Fig. 14 (a) Fitting curves of PFO, (b) PSO, and (c) Langmuir–Hinshelwood models.

Table 3 Parameters of PFO, PSO, and Langmuir–Hinshelwood models

C_0 (mg L^{-1})	Rate constant	R^2
Pseudo-first order		
10	0.06543	0.96509
15	0.04502	0.93578
20	0.03344	0.94054
25	0.0256	0.94859
30	0.02575	0.98217
Pseudo-second order		
10	0.0614	0.97594
15	0.054	0.97554
20	0.0463	0.94808
25	0.0341	0.93992
30	0.0303	0.99965
Langmuir–Hinshelwood		
K (M^{-1})	k_r (min^{-1})	R^2
1.2499	0.00255	0.88751

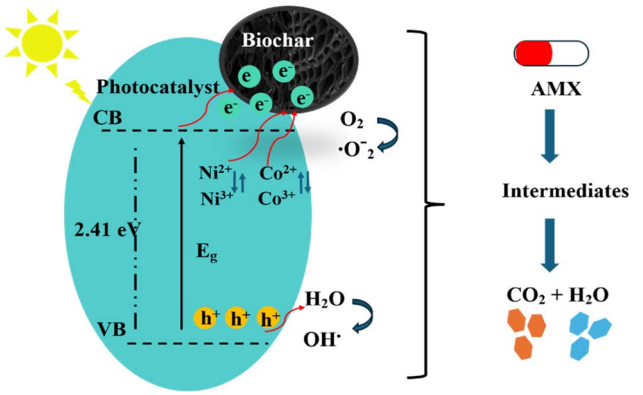

Fig. 15 The proposed photocatalytic degradation mechanism of AMX.

inhibiting charge carrier recombination. In the meantime, Ni^{2+}/Ni^{3+} and Co^{2+}/Co^{3+} redox pairs also enhance charge separation and increase the mobility of electrons and holes. Photogenerated electrons in the conduction band reduce oxygen molecules to generate reactive species while valence band holes promote the oxidation of adsorbed species, resulting in the production of additional reactive radicals. These reactive species assist in the breakdown of organic pollutants. The drug breaks down in stages, with smaller intermediate fragments being produced by the splitting of functional groups like the 2-lactam ring, hydroxyl, amine, and aromatic structures. Through continuing oxidation, these intermediates eventually mineralize into beneficial end products (CO_2, H_2O, and inorganic ions), effectively degrading the antibiotic contaminant.

Conclusions

In summary, the NiCo@BC–MOF derivative was successfully designed as a multifunctional material, ideal for advanced energy storage and environmental purification. Incorporating biochar into the bimetallic MOF framework improves the inherent conductivity limitations of pure MOFs, while the combined effect of the metals further boosts conductivity and the redox properties. The resultant electrode has a balanced energy-power density profile (31.96 Wh kg^{-1} and 287.64 W kg^{-1}) and a notable specific capacitance of 444.44 F g^{-1}. Furthermore, the composite also demonstrated tremendous potential as a photocatalyst in addition to its electrochemical applications. A systematic evaluation of the material under different operating conditions confirmed that a degradation efficiency of 90.1% was achieved. These findings demonstrate the adaptability of NiCo@BC–MOF derivatives for use in promising next-generation SCs and for effective pharmaceutical pollutant remediation in water systems.

Conflicts of interest

There are no conflicts to declare.

Data availability

All data supporting the findings of this study are included within the article. Additional raw data, characterization files, and experimental details are available from the corresponding author upon reasonable request.

Acknowledgements

The authors extend their appreciation to the Vice Deanship of Scientific Research Chairs, King Saud University, Saudi Arabia for funding this research work; Research Chair of Surfactants.

References

1 A. Bhoite, *et al.*, Recent advances in Metal-Organic Framework (MOF) derived metal oxides and their composites with carbon for energy storage applications, *J. Energy Storage*, 2023, **72**, 108557.
2 H. K. Lakeh, What Are the Advantages and Disadvantages of Renewable Energy, *Electronic Besource*, GreenMatch, 2022, vol. 20, p. 2022.
3 U. Shahzad, The need for renewable energy sources, *Energy*, 2012, **2**, 16–18.
4 Y. Liu, *et al.*, Acetylene black enhancing the electrochemical performance of NiCo-MOF nanosheets for supercapacitor electrodes, *Appl. Surf. Sci.*, 2019, **492**, 455–463.
5 T. Mehtab, *et al.*, Metal-organic frameworks for energy storage devices: Batteries and supercapacitors, *J. Energy Storage*, 2019, **21**, 632–646.
6 M. Li, *et al.*, A flower-like Co/Ni bimetallic metal-organic framework based electrode material with superior

performance in supercapacitors, *J. Alloys Compd.*, 2023, **930**, 167354.
7 K. O. Oyedotun, *et al.*, Advances in supercapacitor development: materials, processes, and applications, *J. Electron. Mater.*, 2023, **52**(1), 96–129.
8 D.-G. Wang, *et al.*, Metal-organic framework-based materials for hybrid supercapacitor application, *Coord. Chem. Rev.*, 2020, **404**, 213093.
9 T. Shu, *et al.*, A hydrophobic phenolic polymer layer with high-flux Zn 2+-specific regular channels for stabilizing aqueous zinc anodes, *J. Mater. Chem. A*, 2024, **12**(8), 4666–4677.
10 Q. Sun, *et al.*, Mxene quantum dot insertion-induced electron transfer in CoFe LDH for high-performance zinc-air batteries, *Chem. Eng. J.*, 2025, 164075.
11 L. Phor, A. Kumar and S. Chahal, Electrode materials for supercapacitors: a comprehensive review of advancements and performance, *J. Energy Storage*, 2024, **84**, 110698.
12 A. Bavykina, *et al.*, Metal–organic frameworks in heterogeneous catalysis: recent progress, new trends, and future perspectives, *Chem. Rev.*, 2020, **120**(16), 8468–8535.
13 Y. Zhao, *et al.*, Metal–organic frameworks as photoluminescent biosensing platforms: mechanisms and applications, *Chem. Soc. Rev.*, 2021, **50**(7), 4484–4513.
14 D. Li, *et al.*, Advances and Applications of Metal-Organic Frameworks (MOFs) in Emerging Technologies: A Comprehensive Review, *Glob. Chall.*, 2024, **8**(2), 2300244.
15 B. He, *et al.*, Freestanding metal–organic frameworks and their derivatives: an emerging platform for electrochemical energy storage and conversion, *Chem. Rev.*, 2022, **122**(11), 10087–10125.
16 L. Wang, *et al.*, Metal-Covalent Organic Frameworks: Design Strategy, Structure Feature, and Applications in Energy Storage, *Angew. Chem., Int. Ed.*, 2025, **64**(35), e202513165.
17 K. Wang, *et al.*, Layered CuI-MOFs containing [Mo8O26] 4− clusters as supercapacitor electrode materials, *Chem. Eng. J.*, 2019, **367**, 239–248.
18 B. Xu, *et al.*, Recent progress in metal-organic framework-based supercapacitor electrode materials, *Coord. Chem. Rev.*, 2020, **420**, 213438.
19 H. Liu, *et al.*, Spear-shaped Mn/Ni bimetallic hydroxide derived from metal-organic frameworks as electrode materials for aqueous and all-solid-state hybrid supercapacitors, *Colloids Surf., A*, 2020, **601**, 125011.
20 S. Liu, *et al.*, Bimetallic MOF derived NiMn phosphide for high-performance supercapacitor electrode material, *J. Energy Storage*, 2024, **96**, 112684.
21 E. R. Ezeigwe, *et al.*, MOF-deviated zinc-nickel–cobalt ZIF-67 electrode material for high-performance symmetrical coin-shaped supercapacitors, *J. Colloid Interface Sci.*, 2020, **574**, 140–151.
22 N. L. W. Septiani, *et al.*, Revealing the effect of cobalt content and ligand exchange in the bimetallic Ni–Co MOF for stable supercapacitors with high energy density, *J. Power Sources*, 2024, **603**, 234423.
23 M. Saleem, *et al.*, Exploring new frontiers in supercapacitor electrodes through MOF advancements, *J. Energy Storage*, 2024, **76**, 109822.
24 S. A. Al-Thabaiti, *et al.*, Synthesis of copper/chromium metal organic frameworks-Derivatives as an advanced electrode material for high-performance supercapacitors, *Ceram. Int.*, 2023, **49**(3), 5119–5129.
25 V. Shrivastav, *et al.*, Metal-organic framework derived zirconium oxide/carbon composite as an improved supercapacitor electrode, *Energy*, 2021, **235**, 121351.
26 K. Li, *et al.*, Engineering active sites on nitrogen-doped carbon nanotubes/cobaltosic oxide heterostructure embedded in biotemplate for high-performance supercapacitors, *J. Energy Storage*, 2022, **53**, 105094.
27 D. Yue, *et al.*, Inducing energy storage: Bimetallic MOF-derived Co3O4/NiO nanocomposites for advanced electrochemical applications, *Polyhedron*, 2024, **260**, 117062.
28 H. Guo, *et al.*, Trimesic acid-modified 2D NiCo-MOF for high-capacity supercapacitors, *J. Alloys Compd.*, 2023, **934**, 167779.
29 D. Y. Lee, *et al.*, Unusual energy storage and charge retention in Co-based metal–organic-frameworks, *Microporous Mesoporous Mater.*, 2012, **153**, 163–165.
30 K. Li, *et al.*, Vanadium doping and phosphorus vacancy co-regulation of biotemplate derived three-dimensional cobalt phosphide to enhance pseudocapacitance performance, *Appl. Surf. Sci.*, 2023, **622**, 156950.
31 R. Fu, *et al.*, Titanium-based metal-organic frameworks: Synthesis innovations and multifunctional applications, *Coord. Chem. Rev.*, 2025, **541**, 216832.
32 H. Gholipour-Ranjbar, M. Soleimani and H. R. Naderi, Application of Ni/Co-based metal–organic frameworks (MOFs) as an advanced electrode material for supercapacitors, *New J. Chem.*, 2016, **40**(11), 9187–9193.
33 S. Sundriyal, *et al.*, Enhanced electrochemical performance of nickel intercalated ZIF-67/rGO composite electrode for solid-state supercapacitors, *Int. J. Hydrogen Energy*, 2020, **45**(55), 30859–30869.
34 R. Justinabraham, *et al.*, Copper phosphate-assisted silkworm waste-derived biochar composite for energy storage application, *J. Mater. Sci.*, 2023, **58**(20), 8445–8462.
35 A. Kalla, *et al.*, Biochar: a sustainable and an eco-friendly material for energy storage applications, *Int. J. Green Energy*, 2023, 1–15.
36 C. Sun, *et al.*, Naturally nitrogen-doped self-encapsulated biochar materials based on mouldy wheat flour for silicon anode in lithium-ion batteries, *Electrochim. Acta*, 2023, **450**, 142269.
37 Y. Zheng, C. Yu and L. Fu, Biochar-based materials for electroanalytical applications: An overview, *Green Analytical Chemistry*, 2023, 100081.
38 J. Hong, S.-J. Park and S. Kim, Synthesis and electrochemical characterization of nanostructured Ni-Co-MOF/graphene oxide composites as capacitor electrodes, *Electrochim. Acta*, 2019, **311**, 62–71.
39 T. Dang, *et al.*, Ultrathin hetero-nanosheets assembled hollow Ni-Co-P/C for hybrid supercapacitors with

enhanced rate capability and cyclic stability, *J. Colloid Interface Sci.*, 2020, **577**, 368–378.
40 Z. Shao, *et al.*, Two-step pyrolytic preparation of biochar for the adsorption study of tetracycline in water, *Environ. Res.*, 2024, **242**, 117566.
41 X. Wang, *et al.*, Hydrothermal synthesis of NiCo-based bimetal-organic frameworks as electrode materials for supercapacitors, *J. Solid State Chem.*, 2019, **270**, 370–378.
42 H. Kim, *et al.*, Facile one-pot synthesis of Bimetallic Co/Mn-MoFs@ Rice Husks, and its Carbonization for supercapacitor electrodes, *Sci. Rep.*, 2019, **9**(1), 8984.
43 M. Zahid, *et al.*, Photocatalytic Degradation of Norfloxacin Using Biochar Supported nZVMn/TiO_2 Nanocomposite: Synthesis, Characterization, and Performance Evaluation, *Surf. Interfaces*, 2025, 107034.
44 X. Yang, *et al.*, NiCo-MOF Nanospheres created by the ultra-fast microwave method for use in high-performance Supercapacitors, *Molecules*, 2023, **28**(14), 5613.
45 C. Zhang, *et al.*, Preparation and application of Co3O4-Ni-MOF/MWCNTs hybrid for supercapacitor, *Ionics*, 2021, **27**(8), 3543–3551.
46 A. Taha and S. Daffalla, Biochar derived from palm waste supported greenly synthesized mno2 nanoparticles as a novel adsorbent for wastewater treatment, *Catalysts*, 2023, **13**(2), 451.
47 F. Cao, *et al.*, Synergistic effect of bimetallic NiCo-MOF on foamed nickel for application in high-performance supercapacitors, *CrystEngComm*, 2024, **26**(4), 484–493.
48 Y. Chen, *et al.*, Ferric hydroxide/NiCo-MOF composite materials as efficient electrocatalysts for the oxygen evolution reaction, *Ionics*, 2023, **29**(4), 1285–1300.
49 M. Yasir, *et al.*, Shielding properties of cement composites filled with commercial biochar, *Electronics*, 2020, **9**(5), 819.
50 Z. Z. Chowdhury, *et al.*, Influence of carbonization temperature on physicochemical properties of biochar derived from slow pyrolysis of durian wood (Durio zibethinus) sawdust, *BioResources*, 2016, **11**(2), 3356–3372.
51 J. D. Clogston and A. K. Patri, Zeta potential measurement, *Characterization of Nanoparticles Intended for Drug Delivery*, 2011, pp. 63–70.
52 M. Bellaj, *et al.*, Cationic and anionic dyes adsorption from wastewater by clay-chitosan composite: An integrated experimental and modeling study, *Chem. Eng. Sci.*, 2024, **285**, 119615.
53 A. M. Al-Enizi, *et al.*, Waste polyethylene terephthalate plastic derived Zr-MOF for high performance supercapacitor applications, *Chemosphere*, 2024, **350**, 141080.
54 C. Xu, *et al.*, Binary nickel–cobalt metal–organic frameworks as electrode for high performance pseudocapacitor, *J. Mater. Sci.: Mater. Electron.*, 2019, **30**, 19477–19486.
55 R. Ilangovan, *et al.*, Nanomaterials: Synthesis, physicochemical characterization, and biopharmaceutical applications, in *Nanoscale Processing*, Elsevier, 2021, pp. 33–70.
56 Q. Yang, *et al.*, Ultrathin Co3O4 nanosheet arrays with high supercapacitive performance, *Sci. Rep.*, 2013, **3**(1), 3537.
57 J. Yu, *et al.*, High specific capacitance electrode material for supercapacitors based on resin-derived nitrogen-doped porous carbons, *ACS Omega*, 2019, **4**(14), 15904–15911.
58 P. Thangasamy, S. Shanmuganathan and V. Subramanian, A NiCo-MOF nanosheet array based electrocatalyst for the oxygen evolution reaction, *Nanoscale Adv.*, 2020, **2**(5), 2073–2079.
59 M. Arshad, *et al.*, A Comprehensive Review MOFs and Their Derivatives as High-Performance Supercapacitor Electrodes, *Chin. J. Struct. Chem.*, 2025, 100676.
60 C. Feng, *et al.*, A porous 2D Ni-MOF material with a high supercapacitive performance, *J. Solid State Chem.*, 2018, **265**, 244–247.
61 A. Navarrete, *et al.*, Controlled growth-dependent electrochemical behavior of cobalt and 1, 3, 5 benzene-tricarboxylic acid-based MOFs for efficient supercapacitor applications, *Mater. Chem. Phys.*, 2024, **317**, 129142.
62 X. Hang, *et al.*, The introduction of cobalt element into nickel-organic framework for enhanced supercapacitive performance, *Chin. Chem. Lett.*, 2023, **34**(7), 107787.
63 S. Li, *et al.*, 2D/2D NiCo-MOFs/GO hybrid nanosheets for high-performance asymmetrical supercapacitor, *Diamond Relat. Mater.*, 2021, **115**, 108358.
64 B. Shen, *et al.*, Efficient Fe (III)/Fe (II) cycling triggered by MoO2 in Fenton reaction for the degradation of dye molecules and the reduction of Cr (VI), *Chin. Chem. Lett.*, 2019, **30**(12), 2205–2210.
65 R. Kousar, *et al.*, Catalytic removal of synozol blue dye from aqueous solution through green synthesized iron NPs with H2O2: with addition of ECOSAR and biological investigation, *Chem. Eng. Sci.*, 2025, 122012.
66 M. Khmaissa, *et al.*, Pollution from livestock farming antibiotics an emerging environmental and human health concern: A review, *J. Hazard. Mater. Adv.*, 2024, **13**, 100410.
67 T. Xia, *et al.*, Photocatalytic degradation of organic pollutants by MOFs based materials: A review, *Chin. Chem. Lett.*, 2021, **32**(10), 2975–2984.
68 A. K. Juma, Z. M. A. Merican and A. Haruna, Recent progress of MOF-based photocatalysts for environmental application and sustainability considerations, *Chem. Eng. Res. Des.*, 2024, **208**, 391–435.
69 Q. Wang, *et al.*, Recent advances in MOF-based photocatalysis: environmental remediation under visible light, *Inorg. Chem. Front.*, 2020, **7**(2), 300–339.
70 R. Roushree and R. Haimbodi, Recent Advances in ZnO-Based Nanocomposites for Amoxicillin Photocatalytic Degradation and Adsorption in Wastewater: A Review, *J. Inorg. Organomet. Polym. Mater.*, 2025, 1–38.
71 M. Verma and A. Haritash, Photocatalytic degradation of Amoxicillin in pharmaceutical wastewater: A potential tool to manage residual antibiotics, *Environ. Technol. Innovation*, 2020, **20**, 101072.
72 T. T. Yu, *et al.*, Facile decolorization of methylene blue by morphology-dependence δ-MnO2 nanosheets-modified diatomite, *J. Phys. Chem. Solids*, 2015, **87**, 196–202.

73 M. Zahid, *et al.*, Biochar-derived photocatalysts for pharmaceutical waste removal, a sustainable approach to water purification, *Appl. Surf. Sci. Adv.*, 2025, **26**, 100721.
74 H. A. El Salam and E. M. El-Fawal, Optimized photocatalytic degradation of antibiotics with modified Co-MOF and NiCo-MOF catalysts, *Environ. Processes*, 2024, **11**(3), 40.
75 C. Yang, *et al.*, A novel visible-light-driven In-based MOF/graphene oxide composite photocatalyst with enhanced photocatalytic activity toward the degradation of amoxicillin, *Appl. Catal., B*, 2017, **200**, 673–680.
76 T. J. Al-Musawi, *et al.*, The application of a new recyclable photocatalyst γ-Fe2O3@ SiO2@ ZIF8-Ag in the photocatalytic degradation of amoxicillin in aqueous solutions, *Environ. Monit. Assess.*, 2023, **195**(3), 372.
77 M. Idrees, *et al.*, Advancements in photocatalytic systems for ciprofloxacin degradation, efficiency, mechanisms, and environmental considerations, *J. Mol. Liq.*, 2025, **424**, 127115.
78 A. G. Trovo, *et al.*, Degradation of the antibiotic amoxicillin by photo-Fenton process-Chemical and toxicological assessment, *Water Res.*, 2011, **45**, 1394.
79 X. Bai, *et al.*, Photocatalytic degradation of some typical antibiotics: Recent advances and future outlooks, *Int. J. Mol. Sci.*, 2022, **23**(15), 8130.
80 R. Abazari and A. R. Mahjoub, Amine-functionalized Al-MOF#@ yx Sm2O3–ZnO: a visible light-driven nanocomposite with excellent photocatalytic activity for the photo-degradation of amoxicillin, *Inorg. Chem.*, 2018, **57**(5), 2529–2545.
81 L. Yadav, *et al.*, Insight into efficient photocatalytic degradation of norfloxacin over a simple, economical biochar-based magnetic photocatalyst under solar illumination: a statistical and experimental approach, *Environ. Sci. Pollut. Res.*, 2024, **31**(51), 60971–60987.
82 F. Ullah, *et al.*, Synergistic degradation of toxic azo dyes using Mn-CuO@ Biochar: An efficient adsorptive and photocatalytic approach for wastewater treatment, *Chem. Eng. Sci.*, 2025, **302**, 120844.
83 M. Sheydaei, B. Ayoubi-Feiz and G. Abbaszade-Fakhri, A visible-light active g-C3N4/Ce–ZnO/Ti nanocomposite for efficient photoelectrocatalytic pharmaceutical degradation: Modelling with artificial neural network, *Process Saf. Environ. Prot.*, 2021, **149**, 776–785.
84 A. Fawzy, H. Mahanna and M. Mossad, Effective photocatalytic degradation of amoxicillin using MIL-53 (Al)/ZnO composite, *Environ. Sci. Pollut. Res.*, 2022, **29**(45), 68532–68546.
85 A. Khaleeq, S. R. Tariq and G. A. Chotana, Fabrication of samarium doped MOF-808 as an efficient photocatalyst for the removal of the drug cefaclor from water, *RSC Adv.*, 2024, **14**(15), 10736–10748.
86 Z. U. H. Khan, *et al.*, Electrochemical Advanced Oxidation Processes as a feasible approach towards treatment of pesticides contaminated water and environmental sustainability: A review, *J. Water Proc. Eng.*, 2025, **70**, 107083.
87 A. Raza, *et al.*, Excellent photocatalytic performance against amoxicillin antibiotic and Pt-free hydrogen production using Fe-doped ZnS nanostructures: reaction kinetics and mechanistic insights, *Catalysts*, 2025, **15**(2), 165.
88 L. Zhou, *et al.*, Electro-photocatalytic degradation of amoxicillin using calcium titanate, *Open Chem.*, 2018, **16**(1), 949–955.
89 Y. Zhang, *et al.*, Metal-organic framework-derived multifunctional photocatalysts, *Chin. J. Catal.*, 2022, **43**(4), 971–1000.
90 M. Aftab, *et al.*, Advanced oxidation processes for pesticide degradation: a comprehensive review on the role of nano zero-valent metals and persulfate activation, *RSC Adv.*, 2025, **15**(48), 40619–40654.
91 Y. Bai, *et al.*, A magnetically reusable Ce-MOF/GO/Fe 3 O 4 composite for effective photocatalytic degradation of chlortetracycline, *Phys. Chem. Chem. Phys.*, 2024, **26**(5), 3832–3841.
92 W. Xu, *et al.*, Magnetic composite photocatalyst $NiFe_2O_4$/$ZnIn_2S_4$/biochar for efficient removal of antibiotics in water under visible light: Performance, mechanism and pathway, *Environ. Pollut.*, 2024, **360**, 124602.
93 Z. Yang, *et al.*, Ni, Co-embedded MOF-derived N-doped bimetallic porous carbon for adsorption–photocatalytic degradation of organic dyes and antibiotics, *ACS Omega*, 2024, **9**(10), 11356–11365.